Energy Distribution of a Vehicle Shimmy System with the Delayed Tyre Model ⋆

Tian Mi * **Nan Chen** * **Gabor Stepan** ** **Denes Takacs** ***

* *School of Mechanical Engineering, Southeast University, Nanjing, China (e-mail: mitian@seu.edu.cn; nchen@seu.edu.cn).*
** *Department of Applied Mechanics, Budapest University of Technology and Economics, Budapest, Hungary (e-mail: stepan@mm.bme.hu).*
*** *MTA-BME Research Group on Dynamics of Machines and Vehicles, Budapest, Hungary (e-mail: takacs@mm.bme.hu).*

Abstract: A vehicle shimmy model using the Delayed Tyre Model to estimate the lateral tyre force is introduced. Stability charts are obtained for the linearized system. With reduced damping and stiffness parameters, a new vibration mode shows up at high speed range when the front wheels oscillate in opposite directions. Furthermore, the kinetic energy distributed on each generalized coordinate is calculated at the critical frequencies, and some suggestions are given on how to reduce shimmy in specific cases.

Keywords: vehicle shimmy, Delayed Tyre Model, dynamic modeling, stability chart, energy distribution

1. INTRODUCTION

Vehicle shimmy, also known as "death wobble", is a self-excited vibration of the front wheels around their kingpins. It increases tyre wear, and deteriorates vehicle manoeuvrability.

A series of single wheel shimmy models corresponding to the aircraft landing gear or the trailer problems, have been studied by many researchers. Pacejka (2002) and Ran et al. (2014) use these shimmy models of different levels of complexity, determine the energy flow in the motion with the energy flow method, and compare different tyre models on shimmy. Much analytical and experimental work has been done on the shimmy of a trailer by using the Delayed Tyre Model in Takacs et al. (2009) and Takacs and Stepan (2012).

There is another type of shimmy models corresponding to the ground vehicles. In order to distinguish them from the single wheel models, "vehicle shimmy" is used in this case. Vehicle shimmy models are often built with higher degrees of freedom (DoF), and take into account of the steering and suspension systems. Nonlinearities such as the tyre elasticity, dry friction, and clearance (or freeplay) of the steering system can all be considered. The semi-empirical tyre model – Pacejka's Magic Formula (Pacejka, 2002) is widely used in vehicle shimmy problems, not only for the huge amounts of experimental validation of the tyre model, but also because that the nonlinearity can be introduced into the system in an explicit way, and the resultant ordinary differential equations are relatively easy to solve. For the related models, we refer to Li and Lin (2006), Wei et al. (2015) and Mi et al. (2017).

In this study, a 3 DoF vehicle shimmy model based on Li and Lin (2006) is established along with the Delayed Tyre Model as in Takacs et al. (2009). With the dependent suspension and the simplified steering system, the analytically more accurate tyre model can also be integrated without making the equations too lengthy.

The controller considering shimmy is difficult to design (see Goodwine and Stepan (2000)). In this respect, understanding more about the vibration is of great importance. If we can determine which part of the mechanism influences shimmy the most, and make efforts to attenuate the vibration accordingly, it can be expected that the problem will be easier to deal with. This inspires us to check the energy distribution and to find out the specific parameters which may be used on shimmy control.

The rest of this paper is organized as follows: the dynamic model of the system and the tyre model are explained in section 2; in section 3, the stability charts and the corresponding frequency maps are obtained with the linearized system; the kinetic energy distributions in the generalized coordinates are calculated with different critical frequencies in section 4; finally, conclusions are given in section 5.

2. PROBLEM FORMULATION

2.1 System Modeling

With the assumptions that:

i) the vehicle runs at constant speed on a flat road,
ii) the steering wheel is fixed,

⋆ This research was support by the National Natural Science Foundation of China (number: 51375086) and the China Scholarship Council.

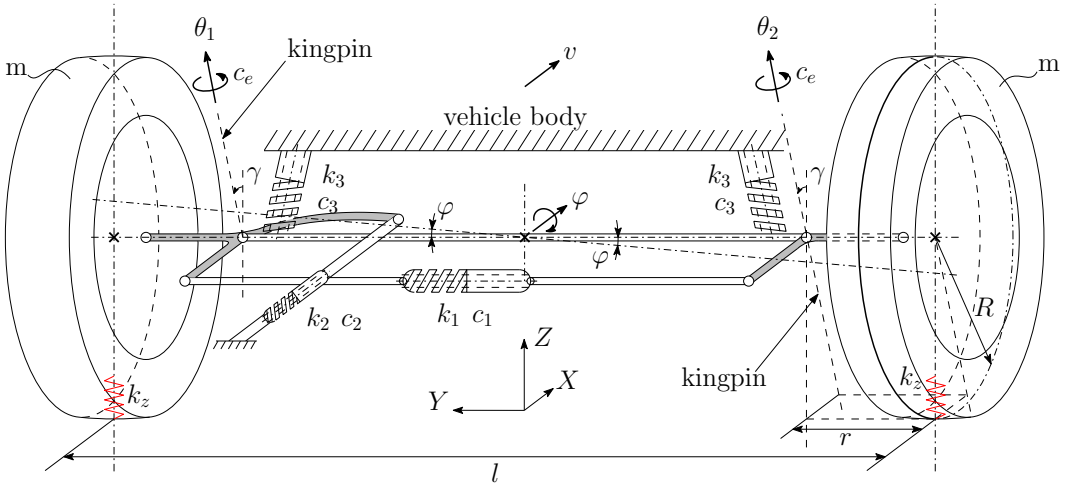

Fig. 1. Mechanical model.

iii) no longitudinal slip occurs between the tyre and road,

a 3 DoF vehicle shimmy model (according to Li and Lin (2006)) is introduced in this section, where the vibrations of the left wheel $\theta_1(t)$ and right wheel $\theta_2(t)$ around their kingpins, and the swing $\varphi(t)$ of the dependent suspension about the longitudinal axis are all taken into account, see Fig. 1.

The equations of motion are given by:

$$\begin{cases} (J_\mathrm{d}+mr^2)\,\ddot{\theta}_1(t)-(J_d+\frac{1}{2}mlr)\,\ddot{\varphi}(t)+(c_1+c_2+\\ +c_\mathrm{e})\,\dot{\theta}_1(t)-c_1\,\dot{\theta}_2(t)+J_0\frac{v}{R}\,\dot{\varphi}(t)+(k_1+k_2)\,\theta_1(t)-\\ -k_1\,\theta_2(t)-\frac{1}{2}k_z lr\gamma\,\varphi(t)=Q_1,\\ (J_\mathrm{d}+mr^2)\,\ddot{\theta}_2(t)-(J_d+\frac{1}{2}mlr)\,\ddot{\varphi}(t)-c_1\dot{\theta}_1(t)+\\ +(c_1+c_\mathrm{e})\,\dot{\theta}_2(t)+J_0\frac{v}{R}\,\dot{\varphi}(t)-k_1\,\theta_1(t)+k_1\,\theta_2(t)-\\ -\frac{1}{2}k_z lr\gamma\,\varphi(t)=Q_2,\\ -(J_\mathrm{d}+\frac{1}{2}mlr)\gamma\,\ddot{\theta}_1(t)-(J_\mathrm{d}+\frac{1}{2}mlr)\gamma\,\ddot{\theta}_2(t)+(2J_\mathrm{d}+\\ +\frac{1}{2}ml^2)\,\ddot{\varphi}(t)-J_0\frac{v}{R}\,\dot{\theta}_1(t)-J_0\frac{v}{R}\,\dot{\theta}_2(t)+c_3\,\dot{\varphi}(t)-\\ -\frac{1}{2}k_z lr\gamma\,\theta_1(t)-\frac{1}{2}k_z lr\gamma\,\theta_2(t)+(k_3+\frac{1}{2}k_z l^2)\,\varphi(t)=Q_3, \end{cases} \tag{1}$$

where Q_1, Q_2, and Q_3 are the generalized forces; J_0, J_d are the mass moments of inertia of a wheel with respect to (w.r.t.) the rolling axle and its diameter, respectively; $c_{1,2,3,\mathrm{e}}$ and $k_{1,2,3,z}$ are damping and stiffness parameters, respectively; R is the rolling radius of the wheel, m is the wheel mass, and γ is the caster angle; see Fig. 1.

2.2 The Delayed Tyre Model

As shown in Fig. 2, the tyre is considered to be thin, thus the contact area decays into a line. Taking the left wheel as an example, the lateral tyre deformation is denoted by $q_1(x,t)$. In the (x,y) plane, L $(a,\, q_1(a,t))$ is the leading point, R $(-a,\, q_1(-a,t))$ is the rear point, and P $(x,\, q_1(x,t))$ is an arbitrary point on the contact line, where a is half of the contact length. With the stretched string-type tyre assumption (Takacs et al., 2009), the tyre deformation within the contact region is not restricted, and outside the contact area decays exponentially. The position of point P is expressed as

$$q_1(x,t)=\begin{cases} q_1(-a,t)e^{(x+a)/\sigma}, & \text{if } x\in(-\infty,-a);\\ q_1(x,t), & \text{if } x\in[-a,a];\\ q_1(a,t)e^{-(x-a)/\sigma}, & \text{if } x\in(a,\infty); \end{cases} \tag{2}$$

where σ is the relaxation length. The generalized forces are then given by

$$\begin{aligned} Q_{1,2}&=k\int_{-\infty}^{\infty}(a-R\gamma)q_{1,2}(x,t)dx,\\ Q_3&=\Big(k\int_{-\infty}^{\infty}q_1(x,t)dx+k\int_{-\infty}^{\infty}q_2(x,t)dx\Big)R, \end{aligned} \tag{3}$$

where k is the lateral tyre stiffness, and $q_2(x,t)$ is the lateral deformation of the right tyre.

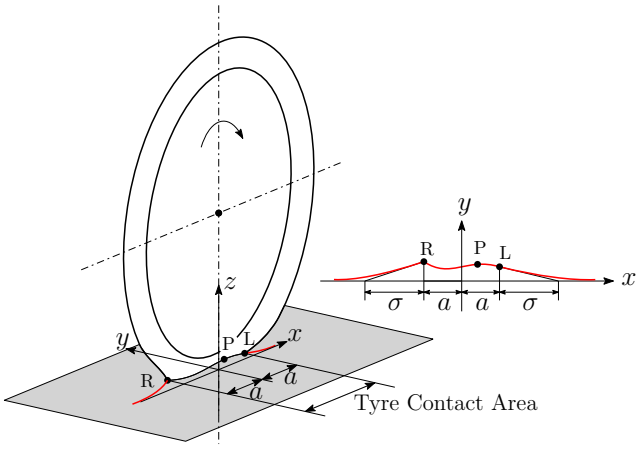

Fig. 2. Stretched string-type tyre.

In a coordinate system (X, Y, Z) fixed on the ground (see Fig. 1), the position of the tyre contact point can be derived by the matrix transformations. The linearized forms of the position vector in X and Y directions are given by

$$X(x,t) = vt - r\theta_1(t) + x,$$
$$Y(x,t) = \frac{l}{2} + q_1(x,t) + (x - R\gamma)\theta_1(t) + R\varphi(t). \quad (4)$$

With assumption iii), the tyre particles stick to the ground in the contact patch, that is,

$$\frac{\mathrm{d}X}{\mathrm{d}t} = 0, \ \frac{\mathrm{d}Y}{\mathrm{d}t} = 0. \quad (5)$$

The substitution of (4) into (5) leads to the expressions of $\dot{x}$ and $\mathrm{d}q_1(x,t)/\mathrm{d}t$. The travelling wave solution is:

$$X(x,t) = X(a, t-\tau), \ Y(x,t) = Y(a, t-\tau), \quad (6)$$

where the delay τ is the time needed for the tyre particle to move from the leading point L to an arbitrary point P on the contact line.

With $\mathrm{d}q_1(x,t)/\mathrm{d}t = \partial q_1(x,t)/\partial t + \dot{x} \cdot \partial q_1(x,t)/\partial x$ and $\partial q_1(a,t)/\partial x = -q(a,t)/\sigma$ at the leading point P, equations (2)-(6) together with (1) give a system which will finally be governed by 3 delay differential equations (DDE) and two ordinary differential equations (ODE).

Note that the ideas are only explained in brief here, for details of the derivation we refer to Takacs et al. (2009) and Mi et al. (2017).

3. STABILITY ANALYSIS

For our system which contains DDEs, there are infinite many eigenvalues, but only a few of them locate in the right half of the complex plane. When the eigenvalues are in the imaginary axis, shimmy can occur in the corresponding nonlinear system. The stability boundary can be obtained by calculating the critical eigenvalues with certain parameter combinations.

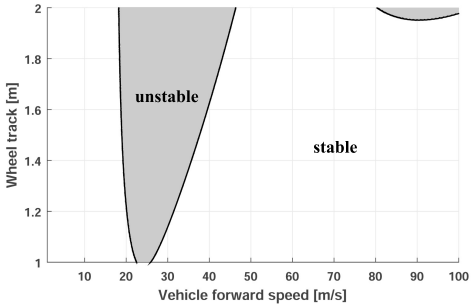

Fig. 3. Stability chart with realistic parameters.

Fixing the vehicle forward speed v and the wheel track l, stability chart for a heavy vehicle (Li and Lin, 2006) is shown in Fig. 3, and the parameters are given in Table. 1. Numerical method – the Bisection Method (Bachrathy and Stepan, 2012) is used due to the high dimension of the system.

In Fig. 3, there are two lobes in the speed ranges of 20-50 m/s and 80-100 m/s, respectively, and the lobe in the larger speed range only shows up a little with very large wheel track though. To investigate more dynamic behaviours, we reduce the damping values $c_{1,2,\mathrm{e}}$ in the steering system and at the kingpins by 0.4, and stiffness values $k_{1,2}$ of the steering system by 0.7. The stability chart and the corresponding critical frequency map are

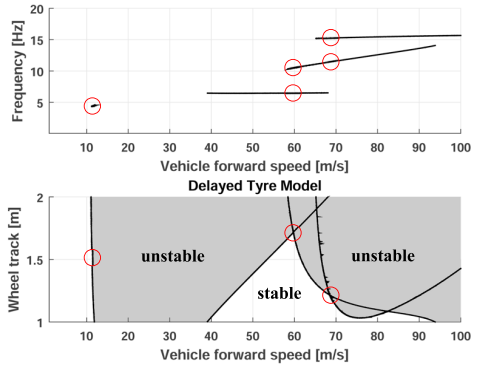

Fig. 4. Stability chart and the corresponding critical frequency map with reduced damping and stiffness of the steering system (and at the kingpins).

shown in Fig. 4, where more complicated vibrations occur. The previously existing two lobes (similar as that in Fig. 3, with frequencies of 5-7 Hz and 10-15 Hz, respectively) come down and their boundaries cross each other, where the quasi-periodic oscillation is expected. A new lobe at very high speed ($>$ 65 m/s) with frequencies of about 15-16 Hz shows up.

The vibration modes of the three selected points (marked with red circles) in Fig. 4 are shown in Fig. 5. Panel (a) is obtained at the point $v = 11.3$ m/s, $l = 1.50$ m in the first lobe (with the lowest frequency of 5-7 Hz), with a critical frequency of 4.4 Hz. Panel (b) and (c) are obtained at the intersection point $v = 59.8$ m/s, $l = 1.71$ m of the first lobe and second lobe (with the critical frequency of 10-15 Hz), and the frequencies are 6.5 Hz and 10.5 Hz, respectively. Panel (d) and (e) are for the intersection point $v = 68.7$ m/s, $l = 1.21$ m of the second lobe and third lobe (with the highest frequency of 15-16 Hz), and the frequencies at different lobes are 11.5 Hz and 15.3 Hz, respectively.

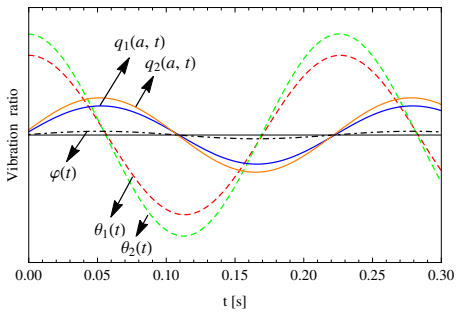

(a) First lobe, $v = 11.3$ m/s, $l = 1.50$ m, and $f = 4.4$ Hz.

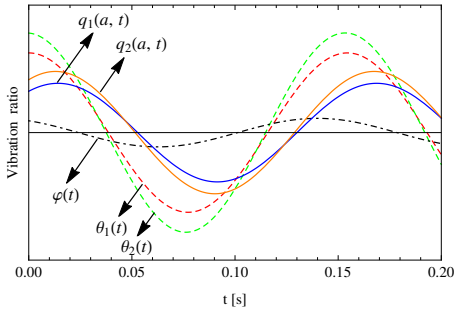

(b) First lobe, $v = 59.8$ m/s, $l = 1.71$ m, and $f = 6.5$ Hz.

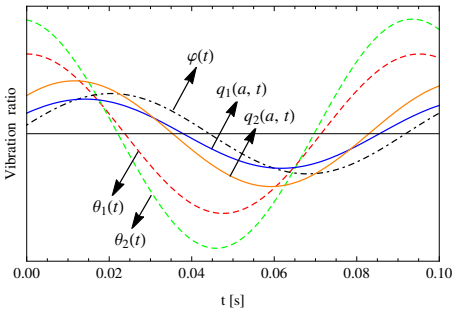

(c) Second lobe, $v = 59.8$ m/s, $l = 1.71$ m, and $f = 10.5$ Hz.

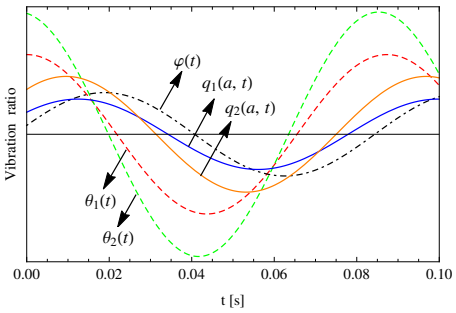

(d) Second lobe, $v = 68.7$ m/s, $l = 1.21$ m, and $f = 11.5$ Hz.

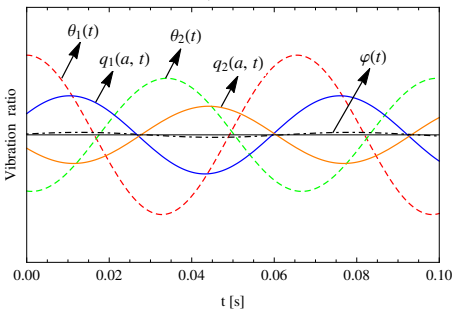

(e) Third lobe, $v = 68.7$ m/s, $l = 1.21$ m, and $f = 15.3$ Hz.

Fig. 5. Vibration modes of the selected points in Fig. 4 with different frequencies.

In the first lobe corresponding to panel (a) and (b), the vibration amplitude of the swing angle $\varphi(t)$ is small, while the shimmy angles of front wheels $\theta_{1,2}(t)$ are much larger. The tiny difference in the amplitudes between left and right wheels is caused by the asymmetry of the system, as depicted in Fig. 1. Compared with panel (a), the vibration amplitude of the swing angle $\varphi(t)$ is larger in panel (b), and the phases of $\theta_{1,2}(t)$ and $\varphi(t)$ are shifted relative to the lateral tyre deformations $q_{1,2}(a,t)$. It can be related to the wide speed range of the lobe. If we trace the vibration modes along the first lobe with realistic parameters in Fig. 3, the phases shift little by little with the increase of the speed, and so does the amplitude increase of $\varphi(t)$. Panel (b) and (c) have very similar vibration modes, where the swing angle $\varphi(t)$ of the suspension vibrates more strongly compared with that in panel (a) and (b).

For the first two lobes, the contact lines $q_1(a,t)$ and $q_2(a,t)$ (or the shimmy angles $\theta_1(t)$ and $\theta_2(t)$) are in the same phase, when the left and right wheels vibrate in the same direction. However, in panel (e) of Fig. 5, the front wheels vibrate in opposite phases.

4. ENERGY DISTRIBUTION

In order to investigate more details of the vibrations, the kinetic energy distributed in each generalized coordinate at different parameter combinations is checked in this part.

The energy of the system are also considered in Pacejka (2002) and Ran et al. (2014) , and the energy flow method is used to compare different tyre models, and to show how the energy flows from different input sources. On contrast, we do not focus on where the energy comes from, but on how it reflects on different coordinates.

The contribution of the ith generalized coordinate to the total kinetic energy (see Shi et al. (2009)) can be calculated as

$$\eta_i(t) = \frac{T_i(t)}{T(t)} = \frac{\sum_{j=1}^{3} J_{ij} q_i(t) q_j(t)}{\sum_{i=1}^{3}\sum_{j=1}^{3} J_{ij} q_i(t) q_j(t)} \times 100\%, \ i = 1, 2, 3, \tag{7}$$

where $T_i(t)$ is the kinetic energy distributed in ith generalized coordinate (i.e. $\theta_1(t)$, $\theta_2(t)$, and $\varphi(t)$), J_{ij} is the element of matrix $\boldsymbol{J}$ in ith row, jth column.

By calculating the eigenvectors of the critical eigenvalues, and substituting them into (7), the energy distributions corresponding to Fig. 5, panel (a)-(e) are pictured in Fig. 6, panel (a)-(e), respectively. Panel (a) and (b) in Fig. 6 show that, the proportion of the front-wheel vibrations is large in the first lobe, although that of the swing angle rises with the increase of the critical frequency. For the second lobe, the vibration of the suspension around the longitudinal axis increases dramatically, see panel (c) and (d). When the third lobe (see panel (e)) constitute the majority of the total energy, just like the first lobe.

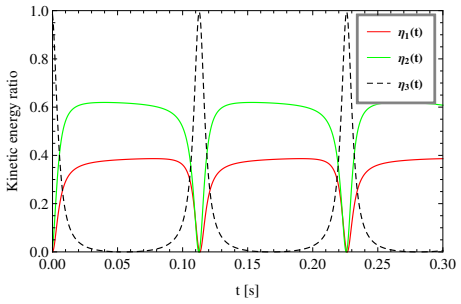

(a) First lobe, $v = 11.3$ m/s, $l = 1.50$ m, and $f = 4.4$ Hz; corresponding to panel (a) of Fig. 5.

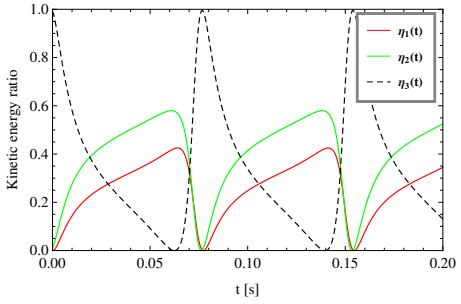

(b) First lobe, $v = 59.8$ m/s, $l = 1.71$ m, and $f = 6.5$ Hz; corresponding to panel (b) of Fig. 5.

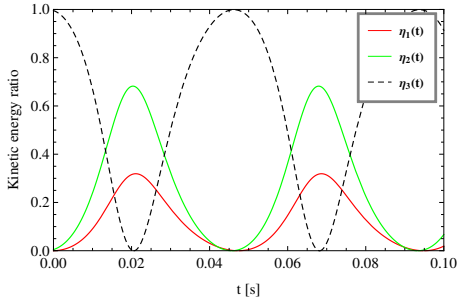

(c) Second lobe, $v = 59.8$ m/s, $l = 1.71$ m, and $f = 10.5$ Hz; corresponding to panel (c) of Fig. 5.

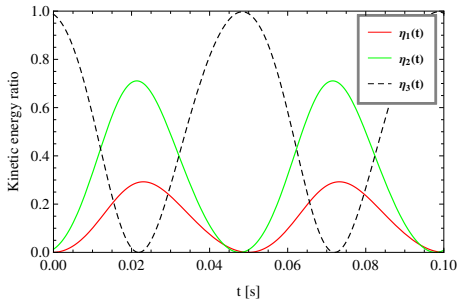

(d) Second lobe, $v = 68.7$ m/s, $l = 1.21$ m, and $f = 11.5$ Hz; corresponding to panel (d) of Fig. 5.

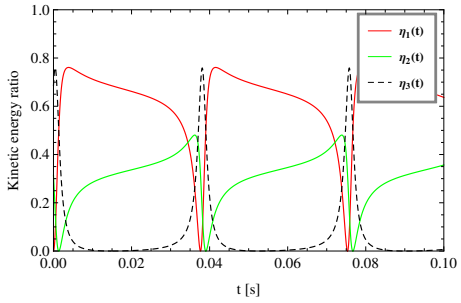

(e) Third lobe, $v = 68.7$ m/s, $l = 1.21$ m, and $f = 15.3$ Hz; corresponding to panel (e) of Fig. 5.

Fig. 6. Energy distributions on gereralized coordinates in different vibration modes corresponding to Fig. 5.

Now it will be interesting to see what happens if some specific damping values in different parts of the system are changed.

When the damping values corresponding to the front-wheel shimmy, that is, $c_{1,2}$ of the steering system or c_e at the kingpins are increased while all the others remain the same with that in Fig. 4, the resulting stability charts and corresponding frequency maps are shown in Fig. 7. Either we increase $c_{1,2}$ (see panel (a) of Fig. 7) or c_e (see panel (b) of Fig. 7) by a factor of 1.5, the third lobe disappears in the shown region. Compared to the stability chart in Fig. 4, the first two lobes almost stand in the same positions – they become a bit smaller indeed but not palpable. It agrees with the energy distribution in panel (e) of Fig. 6.

The stability chart and frequency map with increased damping c_3 of the suspension around longitudinal axis are shown in Fig. 8, where the damping is multiplied by a factor of 1.5 also. This time, the first lobe and third lobe remain but the second lobe goes up.

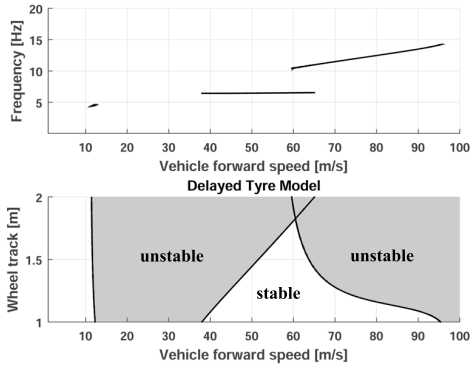

(a) $c_{1,2}$ are increased by a factor of 1.5.

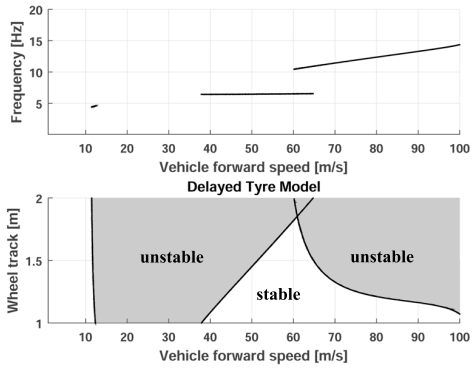

(b) c_e is increased by a factor of 1.5.

Fig. 7. Stability charts obtained with increased damping values of the steering system and at the kingpins.

To conclude, the first lobe is "stubborn", and does not change much with the increase of specific damping value(s). When the total damping is increased, the first lobe goes up, and the unstable region becomes smaller (see Fig. 3). The second lobe is sensitive to the suspension damping (c_3), and the third lobe is sensitive to the damping parameters corresponding to the front-wheel shimmy (i.e. $c_{1,2}$ and c_e).

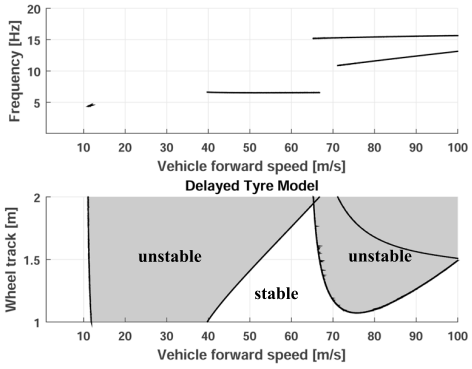

Fig. 8. Stability chart obtained with increased damping value c_3 of the suspension around the longitudinal axis by a factor of 1.5.

Table 1. Parameters in the stability analysis.

Description	Symbol	Value
mass moment of inertia	J_0	4.85 kg m^2
	J_d	6 kg m^2
	J_3	20 kg m^2
damping	c_1	10 N s/(m rad)
	c_2	100 N s/(m rad)
	c_3	1 050 N s/(m rad)
	c_e	44 N s/(m rad)
stiffness	k_1	35 500 N m/rad
	k_2	17 000 N m/rad
	k_3	32 000 N m/rad
	k_z	400 000 N/m
geometric parameters	R	0.4 m
	r	0.07 m
	γ	0.04 rad
tyre-road contact	a	0.2 m
	σ	0.65 m

5. CONCLUSION

In this paper, a 3 DoF shimmy model taking into account the steering system and the suspension system is introduced with the Delayed Tyre Model. Constraint equations are derived with the stretched string-type tyre assumption, which considers the lateral tyre deformation both in and out of the contact patch. The resultant system with delay differential equations is linearized and the stability charts are obtained by numerical method.

For more interesting dynamic behaviours of the system, the damping and stiffness values are reduced. As a result, quasi-periodic oscillations occur, and even a new lobe appears. By determining the eigenvectors corresponding to the critical frequencies at some chosen points in the stability chart, the vibration modes are visualized. It turns out that in the previous existing two lobes, the front wheels vibrate in the same direction, while in opposite phases in the new lobe.

By calculating the kinetic energy distribution in each generalized coordinate, the main energy consuming coordinate(s) can be determined. If we increase the corresponding damping values of the components, the unstable lobes in the high speed range shrink dramatically. However, the lobe with lowest critical frequency stays still.

Although the vibration modes can already provide much information about shimmy, the differences among diverse modes are vague. If we further calculate the kinetic energy of each generalized coordinate, the results show that even the similar looking vibration modes (such as the first and second lobes) can have very different energy distributions, and the attenuation of shimmy can be related to different damping parameters.

With the development of the technology, the maximum speed of ground vehicles is increasing, and the control strategies have been developed in various driving conditions. But shimmy is rarely taken into account in the controller designing. This paper introduces a dynamic model considering steering and suspensions systems, and gives some analytical reference for vehicles, for example, with multiple active dampers, on how to deal with the shimmy problem.

The model is established with many simplifications and assumptions: some geometric parameters such as the camber angle are not considered; the tyre contact length and the relaxation length are taken as constants; the steering wheel is fixed; the translational and rotational movements of many components are neglected, etc. The suggestions on shimmy attenuation are neither direct nor easily achievable, especially with a heavy truck at very high speed. However, from the view point of understanding more about the shimmy phenomenon, this work can still provide some valuable reference in the future research.

ACKNOWLEDGEMENTS

This research was support by the National Natural Science Foundation of China (number: 51375086) and the China Scholarship Council.

REFERENCES

Bachrathy, D. and Stepan, G. (2012). Bisection method in higher dimensions and the efficiency number. *Periodica Polytechnica Mechanical Engineering*, 56(2), 81–86.

Goodwine, B. and Stepan, G. (2000). Controlling unstable rolling phenomena. *Journal of Vibration and Control*, 6(1), 137–158.

Li, S. and Lin, Y. (2006). Study on the bifurcation character of steering wheel self-excited shimmy of motor vehicle. *Vehicle System Dynamics*, 44(sup1), 115–128.

Mi, T., Stepan, G., Takacs, D., and Chen, N. (2017). Shimmy model for electric vehicle with independent suspensions. *Proceedings of the Institution of Mechanical Engineers Part D Journal of Automobile Engineering*, (24), 095440701770128.

Pacejka, H.B. (2002). *Tyre and vehicle dynamics*. Butterworth-Heinemann.

Ran, S., Besselink, I.J.M., and Nijmeijer, H. (2014). Application of nonlinear tyre models to analyse shimmy. *Vehicle System Dynamics*, 52(sup1), 387–404.

Shi, W.K., Fu, J.H., Hao, Y., and Teng, T. (2009). Multi-objective optimization of powertrain mounting based on matlab. In *Computational Intelligence and Industrial Applications, 2009. PACIIA 2009. Asia-Pacific Conference on*, 484–487.

Takacs, D., Orosz, G., and Stepan, G. (2009). Delay effects in shimmy dynamics of wheels with stretched string-like tyres. *European Journal of Mechanics / A Solids*, 28(3), 516–525.

Takacs, D. and Stepan, G. (2012). Micro-shimmy of towed structures in experimentally uncharted unstable parameter domain. *Vehicle System Dynamics*, 50(11), 1613–1630.

Wei, D., Xu, K., Jiang, Y., Chen, C., Zhao, W., and Zhou, F. (2015). Hopf bifurcation characteristics of dual-front axle self-excited shimmy system for heavy truck considering dry friction. *Shock and Vibration,2015,(2015-12-8)*, 2015(1), 1–20.